Letter

Bragg scattering induced laser deflection and electron injection in x-ray laser driven wakefield acceleration in crystals

Xiangyan An,[1,2] Min Chen,[1,2,*] Suming Weng,[1,2] Zhengming Sheng,[1,2,3] and Jie Zhang[1,2,3]

[1]*Key Laboratory for Laser Plasmas (MoE), School of Physics and Astronomy, Shanghai Jiao Tong University, Shanghai 200240, China*

[2]*Collaborative Innovation Center of IFSA, Shanghai Jiao Tong University, Shanghai 200240, China*

[3]*Tsung-Dao Lee Institute, Shanghai Jiao Tong University, Shanghai 200240, China*

(Received 10 August 2022; accepted 24 October 2022; published 22 November 2022)

Propagation of intense ultrashort x-ray laser pulse in a metal crystal and its effects on x-ray laser-driven wakefield acceleration are theoretically and numerically investigated with particle-in-cell simulations, where the bound electron effects are included. New features of laser pulse dissipation due to Bragg scattering have been observed and analyzed. The beat wave generated by the drive laser and scattered laser results in plasma density modulation and subsequent drive laser deflection. Continuous electron injection into the wakefields is also found due to the beat wave. These new features of laser propagation, wake generation, and electron injection provide effective controls on x-ray laser driven wakefield acceleration, where an acceleration gradient as high as 0.75 TV/cm is numerically demonstrated.

DOI: 10.1103/PhysRevResearch.4.L042034

Introduction. Laser wakefield acceleration (LWFA) has achieved significant development since it has been proposed by Tajima and Dawson [1]. An acceleration gradient of GV/cm has been widely demonstrated [2–5]. Electrons have been successfully accelerated to several GeV energies within centimeter distance from the laser-driven wakefields [5–7]. However, due to the dephasing issue, to accelerate electrons to TeV level energy [8,9] by ultrashort, ultraintense laser pulses in the optical wavelength range available today, it needs an acceleration length more than 100 m or staged acceleration [10,11]. Although meter-scale plasma waveguides have been achieved [12], it is still a challenge to make plasma waveguides in ten-meter scale and mitigate laser energy depletion due to wakefield excitation in a long propagation distance. Besides, the low coupling efficiency between stages in current staged acceleration is another limitation when hundreds of stages are required for TeV acceleration.

Since the acceleration field scales as $E_a(\mathrm{V/m}) \approx 96\sqrt{n_0(\mathrm{cm}^{-3})}$ [13], much higher acceleration gradient is expected by using high-density plasmas such as the solid density ($>10^{23}$ cm^{-3}) for which TV/cm acceleration gradient is possible [14]. Recently, acceleration gradients of TV/cm are confirmed in crystals [15], nanotubes [16], and dense plasmas [17–19]. To make efficient wake excitation in the high-density plasma, the duration of the drive pulse should correspondingly be shorter. For typical solid density plasmas, the ultrashort intense drive laser should have a central frequency in the x-ray range. In this case, the effects of the internal crystal-like structure of solid targets would be important. As the wavelength of the drive pulse is close to the crystal constant, laser diffraction and scattering in the crystal structure appear. The usual particle-in-cell (PIC) codes neglect the effects of the unionized internal bound electrons. As a result, the laser diffraction by the bound electrons cannot be properly simulated.

We have recently proposed a combined ion model in the PIC code to model the bound electron effects [20] . In this method, the macroparticle model for ions in the PIC code is a two-body system containing a nucleus and a combined bound electron. The motions of these two parts are determined both by external electromagnetic fields and internal Coulomb fields. Their contributions are also included in electric currents. In this way, the main response contributed by the dipole component is reserved. Based on such a method, together with the ions placed periodically, the x-ray diffraction effects by the crystal structure can be self-consistently simulated in the PIC codes in a comprehensive way. In this Letter, we investigate the propagation of an intense x-ray pulse and x-ray laser wakefield acceleration (XLWFA) of electrons in a metal crystal. A few unique features are found, such as Bragg scattering induced x-ray pulse deflection, electron injection in wakefields, x-ray pulse polarization-dependent wakefield excitation, etc.

Bragg scattering of an intense x-ray pulse. Figure 1(a) shows typical characters of XLWFA. An x-ray laser pulse is incident into a partially ionized crystal, where the ionized electrons and the periodically distributed ions form the plasma. When the strength of the x-ray laser pulse is relativistic (i.e., the normalized vector potential $a_0 = |eE/(m_e\omega_0 c)| \gtrsim 1$), a strong wakefield can be excited in the plasma, which is known as LWFA. However, different from normal laser propagation and wakefield excitation in plasma, when the drive

*minchen@sjtu.edu.cn

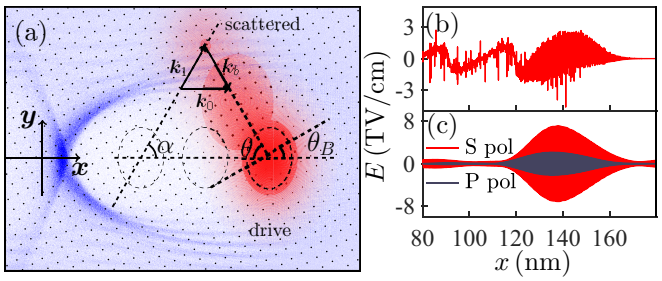

FIG. 1. (a) Schematic of XLWFA in a crystal. The laser is continuously scattered along the angle α (i.e., two times of the Bragg angle θ_B). (b) The distribution of the longitudinal electric field along the line of $y = 0$. (c) The filtered field E_s of the Bragg scattered laser along the center line.

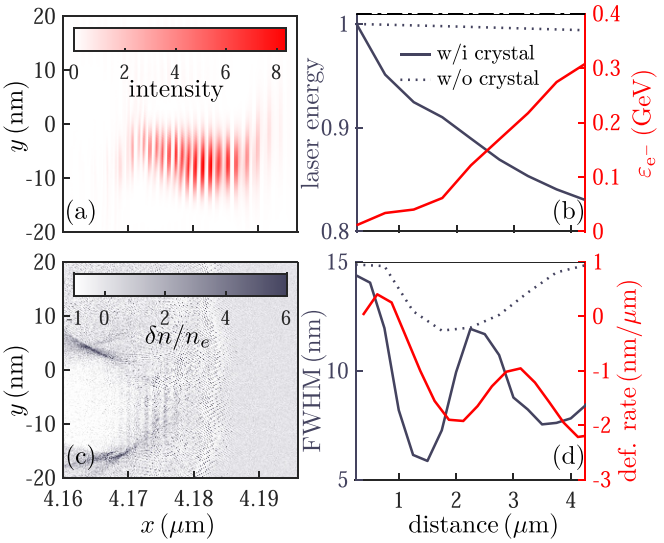

FIG. 2. (a) Normalized intensity of the laser pulse after 4 μm propagation. (b) Evolutions of the remained energy proportion of the drive pulse and the maximum accelerated electron energy. (c) The electron density modulation $\delta n/n_e$ around the drive laser. (d) Evolution of the full width at half-maximum (FWHM) of the drive laser and the deflection rate. The dotted lines in (b) and (d) correspond to the cases without the crystal structure.

laser wavelength is close to the crystal constant and the ions in the lattice are partially ionized, they can coherently scatter the laser, i.e., the Bragg scattering.

We use a typical XFEL laser as the drive laser and take the gold as the target. The lattice constant is $d = 0.26$ nm and the ion number density is $n_0 = 5.9 \times 10^{22}$ cm^{-3}. The normalized vector potential a_0 of the x-ray laser is 3 and the wavelength is the same as the lattice constant $\lambda_0 = d = 0.26$ nm. The corresponding laser electric field and photon energy is 3.7×10^{16} V/m and 4.8 keV, respectively. Since the wake excitation and acceleration are at a spatial scale much larger than the crystal constant, it is not necessary to precisely calculate each atom's ionization. So in our study, the combined electrons with the ionization energy below the photon energy of the x-ray laser are directly ionized and set free in the simulation. We set that each ion has an average ionization degree of $Z_f = 30$ and carries $Z_b = 49$ bound electrons. The corresponding free-electron plasma density is then $n_e = 30n_0$. The x-ray laser beam has Gaussian envelopes in both longitudinal and transverse directions. To resonantly excite strong wakefields, the pulse duration and focus width are $t_L = \lambda_p/(2c)$ and $w_L = \lambda_p/2$, respectively, where $\lambda_p = 2\pi c\sqrt{\frac{\varepsilon_0 m_e}{n_e e^2}} = 25$ nm is the plasma wavelength. Such an x-ray laser pulse contains 24 mJ energy. As a comparison, nowadays FEL in LCLS (Linac Coherent Light Source) can operate with typical parameters as photon energy ~keV, pulse duration ~10 fs, and pulse energy ~mJ [21]. The size of the simulation box is $400\lambda_0 \times 400\lambda_0 \approx 100$ nm $\times$ 100 nm and the grid number is 12000 $\times$ 12000. To show clearly the Bragg scattering effect, in the current simulation, the x-ray laser propagates along the x axis and the crystal axis is set to be at the angle of $\theta_B = \pi/6$. Thus the laser incidence angle with the crystal axis satisfies Bragg's law $\lambda_0 = 2d \sin\theta_B$. The Bragg scattered laser will be at the angle of $\alpha = 2\theta_B = \pi/3$ and along $\boldsymbol{k}_1$ direction, as shown in Fig. 1(a).

Figure 1(b) shows the electric field along the line of $y = 0$. It is a combination of the fields from the drive laser, the scattered laser, and the wakefield. The burr structures on the curve come from the localized fields around the ions. Such structures have also been observed in previous studies [15]. Figure 1(c) shows the Bragg scattered laser field E_s, where $E_s = E_z$ for s-polarized drive laser case and $E_s = E_x \sin\alpha - E_y \cos\alpha$ for p-polarized laser case. Since the laser is scattered in the angle α, the longitudinal projection of the wave vector of the scattered laser is $k_x = k_0 \cos\alpha = 0.5k_0$. To pick out the field of the scattered laser, we made a Fourier transformation of E_s and filtered out the field by selecting $k_x \sim 0.5k_0$. As one can see, the scattered laser is stronger when the drive laser is s polarized. The Bragg scattered laser comes from the coherent superposition of the dipole radiation of each ion in the crystal. Meanwhile, each dipole radiation mainly propagates perpendicularly to the direction of the dipole momentum, which is decided by the polarization of the drive laser. However, in p polarization, the direction determined by Bragg's law is not the main direction of the dipole radiations. So the strength of the Bragg scattered laser is weaker in p polarization. The different scattering intensity finally gives a polarization-dependent XLWFA as one can see in the following.

Deflection of x-ray pulse. Since the laser is continuously scattered by the ions, its propagation and energy evolution are different from that in usual plasmas. The Bragg scattering results in two effects: the drive laser deflection and electron trapping in XLWFA. We first discuss the drive laser deflection. Taking the s-polarized drive pulse as an example, Fig. 2(a) shows the intensity distribution of the laser pulse after 4 μm propagation. As one can see, the laser pulse deviates from its initial propagation axis and the centroid shifts downward. Figure 2(b) also shows that the energy dissipation of the laser pulse is much quicker than the case without the crystal structure. In the latter case, the energy loss is mainly due to the wakefield excitation, which is quite slow. However, in the crystal case, more than 15% energy has been diffracted after 4 μm. At the same time, electrons have been accelerated to 300 MeV in such a short distance. The transverse profile

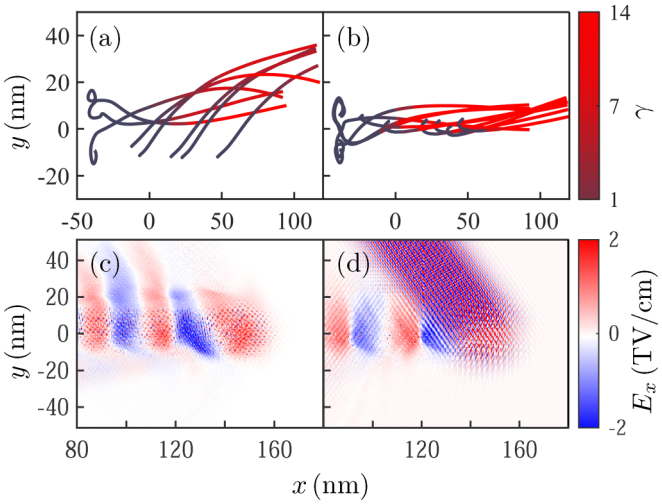

FIG. 3. Typical trajectories of accelerated electrons with an (a) *s*-polarized and a (b) *p*-polarized drive laser. Distribution of the longitudinal electric field E_x with an (c) *s*-polarized and a (d) *p*-polarized drive laser.

evolution of the drive laser can be described as [22]

$$\left(\nabla_\perp^2 + 2ik\frac{\partial}{\partial x}\right)\boldsymbol{a}_0 = k^2\frac{n_e}{n_c\gamma_\perp}\left(1+\frac{\delta n}{n_e}\right)\boldsymbol{a}_0, \qquad (1)$$

where $\gamma_\perp^2 = 1 + \overline{a_0}^2 + 2\overline{\boldsymbol{a}_0}\cdot\overline{\boldsymbol{a}_1}\cos\psi_b$, $\psi_b = (\boldsymbol{k}_0 - \boldsymbol{k}_1)\cdot\boldsymbol{r}$ is the phase of the beat wave, $\overline{\boldsymbol{a}_0}$, $\overline{\boldsymbol{a}_1}$ are the slowly varying amplitudes of the drive and scattered laser averaged over the rapid phase oscillations, respectively, and δn represents the density modulation by the ponderomotive force $-\nabla\gamma_\perp$. Due to the existence of the scattered laser, the transverse symmetry of $\gamma_\perp$ and δn is broken, as shown in Fig. 2(c). Therefore, the drive laser no longer propagates along the $\boldsymbol{x}$ axis but moves downward. Meanwhile, since the transverse self-focusing of the drive laser also relies on $\gamma_\perp$ and δn, it is also different from the usual LWFA case where the crystal structure is absent. The period of focusing and defocusing becomes shorter as shown in Fig. 2(d). It also shows that the drive laser deflects faster when it is defocused.

It is worthwhile to point out that such kind of transverse deflection of the drive laser is due to the plasma response altered by the Bragg scattered laser. In previous studies of LWFA in normal plasma involving two cross pulses, such an effect is not significant since in most cases, the overlapping of the two cross lasers is within a limited region. However, in the current case, the scattered laser overlaps with the drive laser all the time during its propagation, so the effects continuously exist and accumulate.

Electron trapping and acceleration. Along with the drive laser scattering, continuous electron injection has been observed in XLWFA. Figure 3 shows typical trajectories of some injected electrons in the simulation cases with different polarized drive lasers.

As shown in Fig. 3, there are electrons injected from the sharp boundary of the solid target, which have been well studied [15,23,24]. Besides, there are also continuously injected electrons from one side of the laser propagation axis. To find the reason for this kind of injection, we studied the

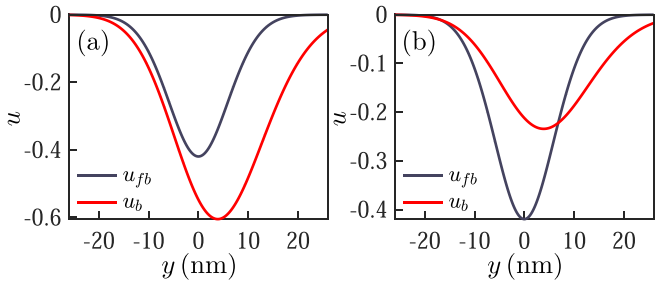

FIG. 4. Comparison of the projection of the background fluid momentum u_{fb} and the critical momentum for electrons trapping in the beat wave u_b for cases with an (a) *s*-polarized drive laser and a (b) *p*-polarized drive laser.

electron dynamics in the fields composed of the drive laser, scattered laser, and the wake. Inside the beat wave formed by the drive laser and scattered laser, the motion of the electron can be described by its Hamiltonian $H(u_b, \psi_b) = \sqrt{\gamma_\perp^2 + u_b^2}$ with respect to the canonical coordinates ψ_b and u_b. See Supplemental Material [25] for the detailed discussion of the electron dynamics, which includes Refs. [13,26].

Since the typical scale lengths of the space variations of $\overline{\boldsymbol{a}_0}$ and $\overline{\boldsymbol{a}_1}$ are both $w_L = \lambda_p/2 \gg \lambda_0$, such large-scale variation could be neglected when one considers the motion of the electron in the beat wave. The separatrix is specified by $H(u_b, \pi) = H(0, 0)$. Thus the maximum and minimum normalized momenta in the $\boldsymbol{k}_b$ direction of the beat wave are [26–29] $u_{b,\pm} = \pm 2\sqrt{\overline{\boldsymbol{a}_0}\cdot\overline{\boldsymbol{a}_1}}$.

Moreover, we can decompose the normalized momentum of the background fluid as $\boldsymbol{u}_f = u_{fb}\hat{\boldsymbol{k}}_b + u_{f\perp}\hat{\boldsymbol{k}}_{b\perp}$, where $\hat{\boldsymbol{k}}_b$ and $\hat{\boldsymbol{k}}_{b\perp}$ are the unit vector along $\boldsymbol{k}_b$ and the direction perpendicular to $\boldsymbol{k}_b$. Then the electron injection is determined by the comparison between u_b and u_{fb}. Since the scattered laser is accumulated from the drive laser, its envelope can be described by the integral of $\overline{\boldsymbol{a}_0}$, while $\overline{\boldsymbol{a}_0}$ and $\boldsymbol{u}_f$ are thought to carry Gaussian envelopes transversely. Meanwhile, the amplitude of $\boldsymbol{u}_f$ can be derived from the wakefield strength [26], which can be obtained from the simulation.

Figure 4 shows the comparison of u_{fb} and u_b [25]. As one can see, for the *s*-polarized drive laser case, u_b is less than u_{fb} in a large region. Therefore, u_{fb} component of the background electrons will be trapped in the direction of $\boldsymbol{k}_b$, while it is still free for $u_{f\perp}$. As a result, u_{fb} component will be averaged to zero when the background electrons move in the beat wave, while $u_{f\perp}$ component is still maintained. Therefore, the background electrons will overall move in the direction of $\hat{\boldsymbol{k}}_{b\perp}$ rather than horizontally. As the motions of the background electrons are twisted, the wakefield will also be twisted, as shown in Fig. 3(c). The wakefield then has the form of $\phi_w = \phi_{w0}\cos(\omega_p t - k_{px}x - k_{py}y)$ and satisfies $k_{px}/k_{py} \approx \cot\theta_B = \sqrt{3}$. Moreover, since the wakefield is excited by the drive pulse, the wavefront still matches the drive pulse and its phase velocity in the x direction is $v_{px} = \omega_p/k_{px} = v_g \approx c$, where v_g is the group velocity of the drive pulse. Therefore, the total phase velocity of the wakefield is thus $v_p = \omega_p/\sqrt{k_{px}^2 + k_{py}^2} \approx \frac{\sqrt{3}}{2}c$. So, the electrons can be injected into the wakefield from

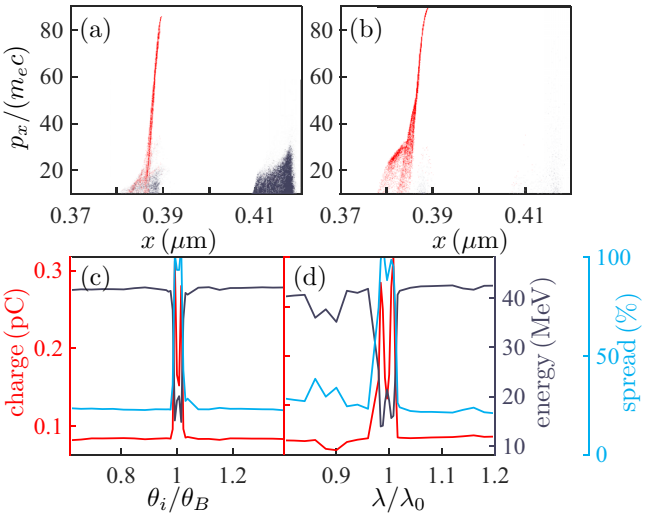

FIG. 5. Distributions of injected electrons in the x-p_x phase space with a p-polarized laser when the incident angle is $\pi/6$ for (a) or $\pi/7$ for (b). The electrons with original positions close to the vacuum-target boundary are labeled in red, while the injected electrons from the inner target are labeled in gray. The total charge, averaged energy, and energy spread of the injected electrons ($p_x > 10 m_e c$) (c) with a fixed wavelength at λ_0 or (d) with a fixed angle at $\pi/6$ after an acceleration distance of 0.5 μm. When calculating the total charge, a length of λ_p is assumed in the imaginary 3rd dimension. When varying the wavelength, the normalized vector potential is fixed.

the side. We refer to such a kind of injection as the scattered laser-assisted electron injection (SLAEI).

For the p-polarized drive pulse case as shown in Fig. 4(b), however, u_b is only less than u_{fb} in the region $y > y_b = 6.8$ nm. Although $u_b < u_{fb}$ holds for the whole region $y > y_b$, the wakefield is too weak to accelerate and focus the electrons far from the y axis. Therefore, in this case, the main part of the wakefield is not disturbed. Only the electrons near y_b can be first trapped by the beat wave and then get trapped by the wakefield.

As Fig. 3 shows, the continuously injected electrons in the case of a p-polarized driver are from the $y > 0$ side and close to the center, which is just the position $y \gtrsim y_b$, while the electrons are injected into the twisted wakefield obliquely in the case of an s-polarized driver.

Control of electron injection. The electrons from different original positions are labeled in Fig. 5(a). One can see that the electrons continuously injected due to the scattered laser are mainly injected into the first bubble, while the electrons injected from the vacuum-plasma boundary are mainly injected into the second bubble. This is because the second and following bubbles behind are far from the scattered laser, so there is no SLAEI. Although SLAEI is an effective electron injection way, there are lots of low-energy electrons in the accelerated beam. Since Bragg's law gives a strict limitation of the wavelength λ and incident angle θ_i, such electrons can be suppressed by breaking the laser crystal matching.

Figures 5(c)–5(d) show the relative charge, averaged energy, and energy spread of the injected electrons after an acceleration distance of 0.5 μm when different incident angle and drive laser wavelength are used. We can see that the SLAEI only happens in a narrow region around $\lambda = 2d \sin\theta_i$. As Fig. 5(b) shows, when Bragg's law is not satisfied, the SLAEI is significantly suppressed while the electrons injected from the boundary are little affected. This provides a flexible way to tune electron beam quality in an x-ray solid target based laser wakefield accelerator and also an evident signal for XLWFA.

Summary. The x-ray laser here needs an XFEL to obtain, requiring long accelerators with huge costs. There are also studies aiming x-ray laser source from laser-plasma interactions [30–32] . Such x-ray laser sources based on laser-plasma interactions also have the potential to realize the XLWFA in this study, which could significantly make it easier to get the x-ray laser.

New features of x-ray laser propagation and wakefield acceleration in a crystal-like solid have been found. It is shown that the energy dissipation would be much faster than that in a usual plasma due to coherent scattering when the laser is incident at the Bragg angle. Meanwhile, the x-ray laser can also be deflected gradually during the propagation. Although the Bragg scattered laser dissipates the drive laser's energy, it can induce continuous electron injection into the wake. Such scattered laser-assisted electron injection will increase the acceleration charge and contribute to the low part of the energy spectrum. These low-quality injections can be suppressed by avoiding the Bragg angle incidence or varying the drive laser wavelength. The acceleration gradient as high as 0.75 TV/cm is confirmed.

This work was supported by the National Natural Science Foundation of China (Grants No. 11991074, No. 12135009, and No. 12225505). The simulations were performed on the π 2.0 supercomputer at Shanghai Jiao Tong University.

[1] T. Tajima and J. M. Dawson, Laser Electron Accelerator, Phys. Rev. Lett. **43**, 267 (1979).

[2] C. G. R. Geddes, C. Toth, J. van Tilborg, E. Esarey, C. B. Schroeder, D. Bruhwiler, C. Nieter, J. Cary, and W. P. Leemans, High-quality electron beams from a laser wakefield accelerator using plasma-channel guiding, Nature (London) **431**, 538 (2004).

[3] S. P. D. Mangles, C. D. Murphy, Z. Najmudin, A. G. R. Thomas, J. L. Collier, A. E. Dangor, E. J. Divall, P. S. Foster, J. G. Gallacher, C. J. Hooker, D. A. Jaroszynski, A. J. Langley, W. B. Mori, P. A. Norreys, F. S. Tsung, R. Viskup, B. R. Walton, and K. Krushelnick, Monoenergetic beams of relativistic electrons from intense laser-plasma interactions, Nature (London) **431**, 535 (2004).

[4] J. Faure, Y. Glinec, A. Pukhov, S. Kiselev, S. Gordienko, E. Lefebvre, J.-P. Rousseau, F. Burgy, and V. Malka, A laser-plasma accelerator producing monoenergetic electron beams, Nature (London) **431**, 541 (2004).

[5] M. Mirzaie, S. Li, M. Zeng, N. A. M. Hafz, M. Chen, G. Y. Li, Q. J. Zhu, H. Liao, T. Sokollik, F. Liu, Y. Y. Ma, L. Chen, Z. M. Sheng, and J. Zhang, Demonstration of self-truncated ionization injection for GeV electron beams, Sci. Rep. **5**, 14659 (2015).

[6] A. J. Gonsalves, K. Nakamura, J. Daniels, C. Benedetti, C. Pieronek, T. C. H. de Raadt, S. Steinke, J. H. Bin, S. S. Bulanov, J. van Tilborg, C. G. R. Geddes, C. B. Schroeder, C. Toth, E. Esarey, K. Swanson, L. Fan-Chiang, G. Bagdasarov, N. Bobrova, V. Gasilov, G. Korn *et al.*, Petawatt Laser Guiding and Electron Beam Acceleration to 8 GeV in a Laser-Heated Capillary Discharge Waveguide, Phys. Rev. Lett. **122**, 084801 (2019).

[7] W. P. Leemans, A. J. Gonsalves, H.-S. Mao, K. Nakamura, C. Benedetti, C. B. Schroeder, C. Toth, J. Daniels, D. E. Mittelberger, S. S. Bulanov, J.-L. Vay, C. G. R. Geddes, and E. Esarey, Multi-GeV Electron Beams from Capillary-Discharge-Guided Subpetawatt Laser Pulses in the Self-Trapping Regime, Phys. Rev. Lett. **113**, 245002 (2014).

[8] W. Leemans and E. Esarey, Laser-driven plasma-wave electron accelerators, Phys. Today **62**, 44 (2009).

[9] C. B. Schroeder, E. Esarey, C. G. R. Geddes, C. Benedetti, and W. P. Leemans, Physics considerations for laser-plasma linear colliders, Phys. Rev. ST Accel. Beams **13**, 101301 (2010).

[10] S. Steinke, J. van Tilborg, C. Benedetti, C. G. R. Geddes, C. B. Schroeder, J. Daniels, K. K. Swanson, A. J. Gonsalves, K. Nakamura, N. H. Matlis, B. H. Shaw, E. Esarey, and W. P. Leemans, Multistage coupling of independent laser-plasma accelerators, Nature (London) **530**, 190 (2016).

[11] J. Luo, M. Chen, W. Y. Wu, S. M. Weng, Z. M. Sheng, C. B. Schroeder, D. A. Jaroszynski, E. Esarey, W. P. Leemans, W. B. Mori, and J. Zhang, Multistage Coupling of Laser-Wakefield Accelerators with Curved Plasma Channels, Phys. Rev. Lett. **120**, 154801 (2018).

[12] B. Miao, L. Feder, J. E. Shrock, A. Goffin, and H. M. Milchberg, Optical Guiding in Meter-Scale Plasma Waveguides, Phys. Rev. Lett. **125**, 074801 (2020).

[13] E. Esarey, C. B. Schroeder, and W. P. Leemans, Physics of laser-driven plasma-based electron accelerators, Rev. Mod. Phys. **81**, 1229 (2009).

[14] T. Tajima and M. Cavenago, Crystal x-ray accelerator, Phys. Rev. Lett. **59**, 1440 (1987).

[15] Z. Liang, B. Shen, X. Zhang, and L. Zhang, High-repetition-rate few-attosecond high-quality electron beams generated from crystals driven by intense X-ray laser, Matter Radiat. Extremes **5**, 054401 (2020).

[16] X. Zhang, T. Tajima, D. Farinella, Y. Shin, G. Mourou, J. Wheeler, P. Taborek, P. Chen, F. Dollar, and B. Shen, Particle-in-cell simulation of x-ray wakefield acceleration and betatron radiation in nanotubes, Phys. Rev. Accel. Beams **19**, 101004 (2016).

[17] Y.-M. Shin, D. A. Still, and V. Shiltsev, X-ray driven channeling acceleration in crystals and carbon nanotubes, Phys. Plasmas **20**, 123106 (2013).

[18] S. Hakimi, X. Zhang, C. Lau, P. Taborek, F. Dollar, and T. Tajima, X-ray laser wakefield acceleration in a nanotube, Int. J. Mod. Phys. A **34**, 1943011 (2019).

[19] A. A. Sahai, T. Tajima, P. Taborek, and V. D. Shiltsev, Solid-state tube wakefield accelerator using surface waves in crystals, Int. J. Mod. Phys. A **34**, 1943009 (2019).

[20] X. An, M. Chen, Z. Sheng, and J. Zhang, Modeling of bound electron effects in particle-in-cell simulation, Commun. Comput. Phys. **32**, 583 (2022).

[21] https://lcls.slac.stanford.edu/parameters

[22] E. Esarey, P. Sprangle, J. Krall, and A. Ting, Self-focusing and guiding of short laser pulses in ionizing gases and plasmas, IEEE J. Quantum Electron. **33**, 1879 (1997).

[23] S. Bulanov, I. Inovenkov, N. Naumova, and A. Sakharov, Excitation of a relativistic Langmuir wave and electron acceleration through the action of an electromagnetic pulse on a collisionless plasma, Sov. J. Plasma Phys. **16**, 444 (1990).

[24] X.-Z. Zhu, W.-Y. Liu, and M. Chen, Effects of slant angle of sharp plasma-vacuum boundary on electron injection in laser wakefield acceleration, Acta Phys. Sin. **69**, 035201 (2020).

[25] See Supplemental Material at http://link.aps.org/supplemental/10.1103/PhysRevResearch.4.L042034 for the detailed discussion of the electron injection dynamics.

[26] G. Fubiani, E. Esarey, C. B. Schroeder, and W. P. Leemans, Beat wave injection of electrons into plasma waves using two interfering laser pulses, Phys. Rev. E **70**, 016402 (2004).

[27] E. Esarey, R. F. Hubbard, W. P. Leemans, A. Ting, and P. Sprangle, Electron Injection into Plasma Wakefields by Colliding Laser Pulses, Phys. Rev. Lett. **79**, 2682 (1997).

[28] X. Davoine, E. Lefebvre, C. Rechatin, J. Faure, and V. Malka, Cold Optical Injection Producing Monoenergetic, Multi-GeV Electron Bunches, Phys. Rev. Lett. **102**, 065001 (2009).

[29] Z. M. Sheng, W. M. Wang, R. Trines, P. Norreys, M. Chen, and J. Zhang, Mechanisms of electron injection into laser wakefields by a weak counter-propagating pulse, Eur. Phys. J.: Spec. Top. **175**, 49 (2009).

[30] N. M. Naumova, J. A. Nees, I. V. Sokolov, B. Hou, and G. A. Mourou, Relativistic Generation of Isolated Attosecond Pulses in a λ^3 Focal Volume, Phys. Rev. Lett. **92**, 063902 (2004).

[31] J. M. Mikhailova, M. V. Fedorov, N. Karpowicz, P. Gibbon, V. T. Platonenko, A. M. Zheltikov, and F. Krausz, Isolated Attosecond Pulses from Laser-Driven Synchrotron Radiation, Phys. Rev. Lett. **109**, 245005 (2012).

[32] Q. Z. Lv, E. Raicher, C. H. Keitel, and K. Z. Hatsagortsyan, High-Brilliance Ultranarrow-Band X Rays via Electron Radiation in Colliding Laser Pulses, Phys. Rev. Lett. **128**, 024801 (2022).